

PHOTONICS Research

In-plane excitation of a topological nanophotonic corner state at telecom wavelengths in a cross-coupled cavity

XIN-TAO HE,^{1,2,†} MENG-YU LI,^{1,2,†} HAO-YANG QIU,^{1,2} WEN-SHENG RUAN,^{1,2} LI-DAN ZHOU,¹ LIN LIU,¹ XIAO-DONG CHEN,^{1,2} WEN-JIE CHEN,^{1,2} FU-LI ZHAO,^{1,2} AND JIAN-WEN DONG^{1,2,*}

¹State Key Laboratory of Optoelectronic Materials and Technologies, Sun Yat-sen University, Guangzhou 510275, China

²School of Physics, Sun Yat-sen University, Guangzhou 510275, China

*Corresponding author: dongjwen@mail.sysu.edu.cn

Received 13 January 2021; revised 28 April 2021; accepted 18 May 2021; posted 20 May 2021 (Doc. ID 419569); published 8 July 2021

In silicon photonics, the cavity mode is a fundamental mechanism to design integrated passive devices for on-chip optical information processing. Recently, the corner state in a second-order topological photonic crystal (PC) rendered a global method to achieve an intrinsic cavity mode. It is crucial to explore such a topological corner state in silicon photonic integrated circuits (PICs) under in-plane excitation. Here, we study both theoretically and experimentally the topological nanophotonic corner state in a silicon-on-insulator PC cavity at a telecommunications wavelength. In theory, the expectation values of a mirror-flip operation for the Bloch modes of a PC slab are used to characterize the topological phase. Derived from topologically distinct bulk polarizations of two types of dielectric-vein PCs, the corner state is induced in a 90-deg-bend interface, localizing at the corner point of real space and the Brillouin zone boundary of reciprocal space. To implement in-plane excitation in an experiment, we fabricate a cross-coupled PC cavity based on the bend interface and directly image the corner state near 1383 nm using a far-field microscope. Finally, by means of the temporal coupled-mode theory, the intrinsic Q factor of a cross-coupled cavity (about 8000) is retrieved from the measured transmission spectra. This work gives deterministic guidance and potential applications for cavity-mode-based passive devices in silicon PICs, such as optical filters, routers, and multiplexers. © 2021 Chinese Laser Press

<https://doi.org/10.1364/PRJ.419569>

1. INTRODUCTION

The optical cavity mode is a fundamental mechanism for light manipulation and light–matter interaction at nanoscale [1]. In silicon photonics, the implementation of passive devices, such as on-chip optical filters, routers, and multiplexers, is highly relevant to the control capability of cavity modes. A photonic crystal (PC) slab provides a useful tool to manipulate cavity modes in silicon photonic integrated circuits (PICs), through finely engineering point defects in the precise location of the PC slab [2,3]. This local method enables us to flexibly control the cavity modes in an extrinsic way, along with increasing the design complexity. Due to recent advances of topological photonics [4–6], a 2D PC slab provides a standard and advanced platform to experimentally explore a variety of topological crystalline phases that are difficult to implement in atomic scale [7–13], and gives a new paradigm to design novel devices in PICs [14–19]. One can apply the simple topology language to achieve an intrinsic cavity mode with a global method [17,20] (i.e., the cavity mode will be induced by the global feature of topological bulk states). In other words, such an

intrinsic cavity mode is totally predictable by investigating the bulk topology, regardless of the local region of PC slab.

In 2D topological photonics [21,22], there are two strategies to design an optical cavity. One is the first-order topological phase that a 2D PC with 2D insulating bulk states supports 1D topological edge states. Due to the robust propagation of edge states along the sharp-bending interface, it is possible to achieve a whispering-gallery-mode ring cavity with an arbitrary profile [20,23,24]. Another is the second-order topological phase, in which a 2D PC with a 2D insulating bulk states supports 0D topological corner states [25–31]. Such 0D corner states with in-plane localization will induce a small-mode-volume cavity mode, and thus the cavity size can be reduced for miniaturization. Nowadays, based on III–V semiconductor materials, the second-order topological photonic crystal (SOTPC) slab has been extensively explored for light–matter interaction [17,32–35], such as light emission of quantum dots, lasing, and quantum electrodynamics. On the other hand, exploration of second-order corner states in silicon PICs is important for the design of a cavity and its passive devices. To do this, two main

issues must be overcome: (i) how to quantitatively determine the second-order topological phase (i.e., bulk polarization) in a PC slab, and (ii) how to experimentally couple the corner state by propagating waves along waveguides (i.e., in-plane excitation), so it can be compatible with other integrated devices.

In this work, a physics quantity of Bloch-mode symmetry with respect to a mirror-flip operation is proposed to evaluate the bulk polarization of SOTPC in theory, and to experimentally observe the topological nanophotonic corner state in a cross-coupled cavity at a telecommunications wavelength. Two types of dielectric-vein PCs, with topologically distinct bulk polarizations, are designed on a standard silicon-on-insulator (SOI) platform that allows integration with other optoelectronic devices in a silicon PIC. In simulation, the nanophotonic corner state in a 90-deg-bend interface constructed by such two topologically distinct PCs is characterized by the local density of state spectra, mode pattern, and 2D spatial Fourier transformation. To experimentally observe the corner state, we fabricate a cross-coupled PC cavity based on the bend interface of SOTPC and image the corner state via a far-field microscope. In addition, we measure the transmission spectra of the interface to characterize the cross-coupled cavity property via a temporal coupled-mode theory.

2. RESULTS

A. Second-Order Topological Photonic Crystal in a Silicon Membrane

Here, the second-order topological structure is designed by a dielectric-vein PC, whose unit cell consists of four square-hole clusters in a silicon background, as shown in Fig. 1. In theory, such an SOTPC can be preliminarily described by the 2D Su-Schrieffer-Heeger (SSH) model [36,37], which gives a clear picture to analyze the intrinsic mechanism. The topology of SOTPC is related to the mirror symmetry of its eigenfields at high-symmetry k points (e.g., Γ , X , Y), which is dominant for the nearest-neighboring hoppings. To simplify in the following discussion, we only focus on two cases of nearest-neighboring hopping (i.e., intra-neighboring hopping t_a dependent on intra-cluster distance d_a and inter-neighboring hopping t_b dependent on inter-cluster distance d_b). For $d_a = d_b = a/2$ [as yellow points in Fig. 1(a)], there are equivalent hopping ($t_a = t_b$) between intra-neighboring and inter-neighboring clusters that the band structure shows as a four-fold degenerate point at X , as well as gives a double degenerated line along the Brillouin zone boundary (i.e., $X-M$). Appendix B has more details about band structures. To open a band gap, one can shrink/expand the clusters to the center/corner of unit cell, so that the structure will generate inequivalent hoppings between inter- and intra-clusters. The shrunk structure (blue) is dominant for intra-cluster hopping ($t_a > t_b$), while the expanded case (red) is for inter-cluster hopping ($t_a < t_b$). In terms of the specific condition that $d_a + s = a$ (or $d_b + s = a$), the intra-clusters (or inter-clusters) can be reconsidered as a new square hole with side length double to $2s$. This type of specific case can help precise nanofabrication avoid approximate separation between two nearest-neighboring clusters. Such a model gives a brief guidance for the practical design of SOTPCs.

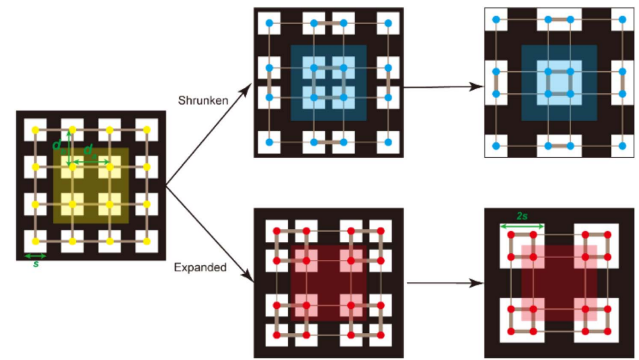


Fig. 1. 2D Su-Schrieffer-Heeger (SSH) model to describe SOTPCs with four square-holes clusters. To shrink/expand the clusters to the center/corner of unit cell, the structure will generate inequivalent inter-intra hopping ($t_a \neq t_b$). The shrunk structure (blue) is dominant for intra-cluster hopping ($t_a > t_b$) with trivial topology, while the expanded case (red) is for inter-cluster hopping ($t_a < t_b$) with nontrivial topology.

In SOTPC design, we consider a dielectric-vein PC slab based on a free-standing silicon membrane (the refractive index of silicon is $n_{\text{Si}} = 3.464$) with 220 nm thickness, as shown in Fig. 2(a). Blue and red boxes indicate shrunk and expanded unit cells, in correspondence with the depiction of Fig. 1. The square holes (side length $2s = 266$ nm) are arranged in square lattice with the periodicity of $a = 430$ nm. For practical PC, the details of bands and eigenmodes are beyond the 2D SSH model with nearest-neighboring hopping. In our calculation, we perform the 3D plane wave expansion method to accurately simulate the band structures [38]. Figure 2(b) shows the

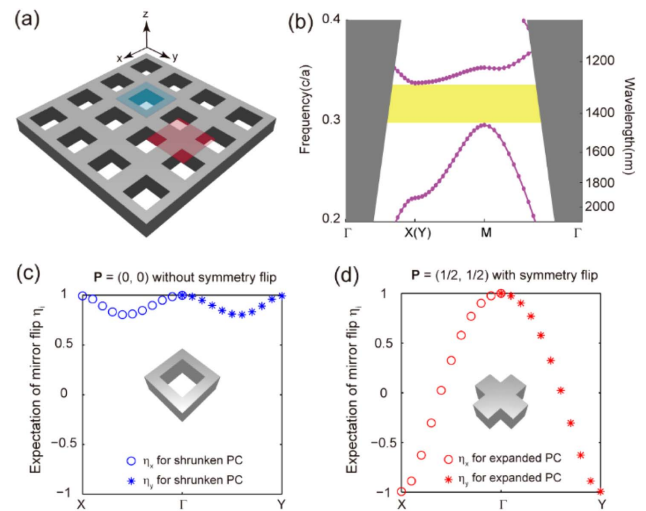


Fig. 2. Bulk states of SOTPC in a silicon membrane. (a) 3D schematic of the designed SOTPC in free-standing silicon membrane with 220 nm thickness. It can be viewed as a dielectric-vein PC in a square lattice with the periodicity $a = 430$ nm and the side length of square holes $2s = 266$ nm. (b) TE-like band structure of SOTPC, showing a 13.2% TE-like gap from 1274 to 1454 nm (yellow). (c)–(d) Expectation values of mirror-flip operation for shrunk PC and expanded PC eigenmodes along ΓX (circle) and ΓY (asterisk) directions. η_x (η_y) represents the expectation values of mirror-flip operation with respect to $x = 0$ ($y = 0$) plane.

TE-like bulk band structure, possessing a 13.2% TE-like gap from 1274 to 1454 nm [as shown in the yellow box in Fig. 2(b)]. The gray region in the band structure represents a light cone of air.

We should emphasize that the topology of an expanded PC is quite different from that of a shrunken PC, although they share the same band structure. Such second-order topological phase can be characterized by bulk polarization \mathbf{P} . $\mathbf{P} = (P_x, P_y)$ is a vector quantity defined by the integration of a Berry connection over the first Brillouin zone. Due to the inversion symmetry constraints on \mathbf{P} , we can have a simple form to determine bulk polarization with respect to the parities at high-symmetry wavevector points (i.e., Γ, X, Y) [39]:

$$P_x = \frac{-i}{2\pi} \ln \left[\prod_{n \in \text{occ}} \frac{\eta_x^n(X)}{\eta_x^n(\Gamma)} \right], \quad P_y = \frac{-i}{2\pi} \ln \left[\prod_{n \in \text{occ}} \frac{\eta_y^n(X)}{\eta_y^n(\Gamma)} \right], \quad (1)$$

where $\eta_i^n(k) = \langle u_n(k) | \hat{\sigma}_{i=0} | u_n(k) \rangle / \langle u_n(k) | u_n(k) \rangle$ is the expectation value of mirror-flip operation $\hat{\sigma}_{i=0}$ with respect to the $i = 0$ plane. i represents x or y axis, $u_n(k)$ is the Bloch function of n -th-band eigenfields at k point and the subscript ‘occ’ in Eq. (1) implies the summation over the bands below the bandgap based on bulk-edge correspondence. In regard to our designed PCs, there is only one TE-like passing band below the topological bandgap. At Γ point, the bulk state of the first TE band is a zero-frequency mode, which is always homogeneous in real space, such that $\eta_i^1(\Gamma) \equiv 1$. Thus, the expression of bulk polarization can be simplified as

$$\mathbf{P} = (P_x, P_y) = \left(\frac{-i}{2\pi} \ln[\eta_x(X)], \frac{-i}{2\pi} \ln[\eta_y(Y)] \right), \quad (2)$$

where η_i represents $\eta_i^n(k)$ of the first band and the superscript 1 is ignored here. In other words, one can estimate the bulk polarization based on the mode symmetry at X and Y points.

To determine the second-order topological phase in PCs, a general method is to “see” the eigenmode distributions and qualitatively judge the parity at high-symmetry k points according to their symmetry. In this work, the expectation value of a mirror-flip operator provides a global parameter to quantitatively evaluate the parity and topological phase. To prove the prediction above, we plot the expectation values of mirror-flip operation of a shrunken PC [as in Fig. 2(c)] and an expanded PC [as in Fig. 2(d)], calculated from their eigenmodes. Circle points represent η_x along ΓX direction, while asterisk points are for η_y along ΓY direction. For shrunken PC with $t_a > t_b$, the mirror-flip operation eigenvalues η_i are always positive. It is a lack of mode-symmetry inversion from Γ to X (Y) points so that the shrunken PC has trivial phase with zero bulk polarization $\mathbf{P} = (0, 0)$. On the other hand, due to $t_a < t_b$ in expanded PC, the inversion symmetry at X (Y) will change to be “odd” compared to the “even” mode at Γ , and thus the expanded PC has a nontrivial phase with nonzero bulk polarization $\mathbf{P} = (1/2, 1/2)$. Therefore, the expectation value of mirror-flip operation is a deterministic parameter to quantitatively evaluate the second-order topological phase in PC, particular for the 3D slab whose eigenmode distributions are more complex than the 2D effective model.

B. Localized Cavity Mode Based on the Topological Corner State

For the second-order topological phase, one essential feature is that a 2D PC with nontrivial bulk polarization supports a 0D topological corner state. As schematically shown in Fig. 3(a), when considering a 90-deg-bend interface constructed by shrunken (blue) and expanded (red) PCs, the corner state will be induced by the differences in bulk polarizations.

To confirm the corner state in simulation, a general method is used to distinguish the eigenmode of corner state from other eigenmodes within the bandgap. This method is applicable for the 2D model, whereas it is not as straightforward to be generalized into a 3D PC slab because the corner state in a PC slab is buried in lots of additional air modes. On the other hand, the corner state is a high- Q cavity mode, so we can investigate its Purcell enhancement phenomena, which can be demonstrated by the local density of states (LDOS) feature. By exciting a dipole source in the FDTD simulation, one can accumulate the time domain Fourier transforms of the field at a given real-space point to obtain the entire LDOS spectrum in a single calculation [40,41]. Figure 3(b) gives the LDOS spectra at the corner point of bend interface, which is normalized by the LDOS in vacuum. The spectrum is excited by a dipole source at the corner point. There is a resonant mode at $\lambda = 1400.515$ nm within the bandgap (yellow region), which is in correspondence

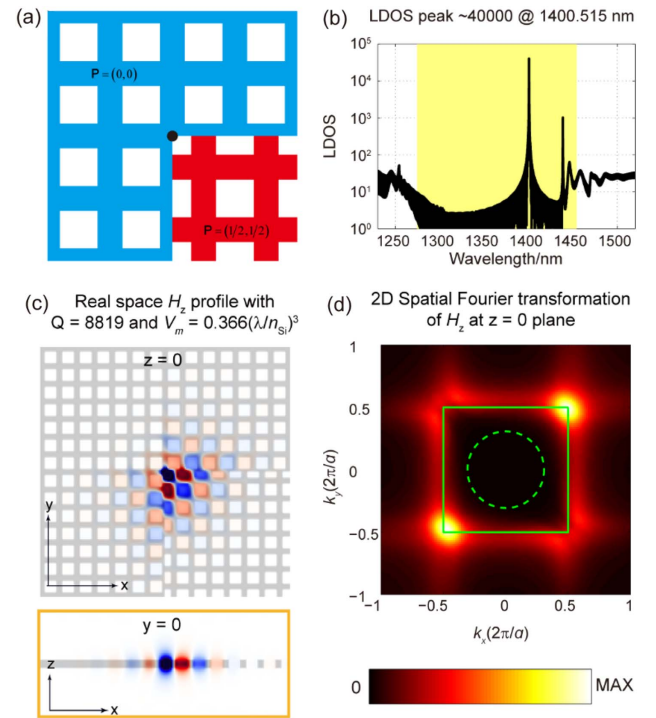


Fig. 3. Localized cavity mode based on topological corner state in a 90 deg bend interface. (a) Schematic illustration of a bend interface constructed by shrunken (blue) and expanded (red) PCs. (b) Photonic LDOS spectrum at the corner point of the bend interface, which is normalized by the LDOS in vacuum. (c) H_z field patterns of corner states for the z center ($z = 0$) and y center ($y = 0$) planes, excited by a dipole source at the corner point at resonant wavelength ($\lambda = 1400.515$ nm). (d) 2D spatial Fourier transformation (FT) of H_z at the z center plane. The green solid box and dashed circle are the first Brillouin zone and light cone of air, respectively.

with topological corner state. The peak value that represents the LDOS at the corner can be enhanced 40,000 times more than in vacuum.

Next, we will focus on the resonant mode distributions in both the real space and momentum space. Figure 3(c) gives the H_z field patterns at a resonant wavelength ($\lambda = 1400.515$ nm) for $z = 0$ and $y = 0$ planes, respectively. The mode energy is mainly confined around the corner of bend interface in 3D. At this mode, the calculated Q factor is about 9000, while the mode volume is $V_m = 0.366(\lambda/n_{\text{si}})^3$. Note that the effect of the 0D corner state works on in-plane confinement, while the vertical confinement should be induced by the total internal reflection (TIR) of the PC slab. To further investigate the strength of the vertical confinement by TIR, we extract the excitation H_z fields with various wavevectors by a 2D spatial Fourier transformation (FT) [3,42]. Figure 3(d) gives the 2D spatial FT spectrum of H_z at the z center plane. The green solid box and dashed circle are the first Brillouin zone and light cone of air, respectively. In the FT spectrum, the wavevector components of the excitation fields are mainly distributed along Brillouin zone boundary, in particular, for the up (right) and down (left) M points. It is because the photonic bandgap opens from the X - M degenerated bands (see Appendix B). According to a little component in the out-of-plane leaky region (inside the green dashed circle), it is accessible to engineer a 3D-confined cavity mode from the topological corner state. In the next section, we will experimentally explore the corner state.

C. Far-Field Microscope Images of the Corner State in a Cross-Coupled Cavity

In the experiment, one of the key issues is how to excite the 3D-confined corner state. This work aims to discuss in-plane excitation of the topological corner state in an SOI platform, which is promising for integrated passive devices. As shown in Fig. 4(a), we design a cross-coupled cavity based on the SOTPC bend interface, of which some edge rectangular holes are filled with silicon to form a line-defect photonic crystal waveguide (PCW). The incident waves propagate along the strip waveguide (waveguide width $w_g = 430$ nm) and line-defect PCW, and then excite the corner state when the coupling length l_{cp} is proper. Here, $l_{\text{cp}} = 5a$. By employing an advanced nanofabrication technique, Fig. 4(b) shows the scanning electron microscope (SEM) images of fabricated samples containing 40×40 PC unit cells. The sample was patterned on a standard 220 nm thick silicon layer based on an SOI platform, but the SiO_2 layer below the PC pattern has been removed to avoid TM-TE coupling of localized fields. Insets give more details about the sample. The lattice constant is almost the same as the design (i.e., $a = 430$ nm) and the side length of the square holes is $2s = 270$ nm. More details about the nanofabrication process can be seen in Appendix A.2.

For optical testing, a fiber-to-chip alignment system with a far-field microscope is applied to characterize the topological nanophotonic corner state (see Appendix A.3). A near-IR (NIR) continuous wave was firstly launched into a fiber polarizer to select the TE mode, and then coupled to the device with the aid of a lensed fiber. After passing through device, the out-of-plane radiation signals were collected by a $100\times$ microscope objective and then imaged using an InGaAs CCD. Figure 4(c)

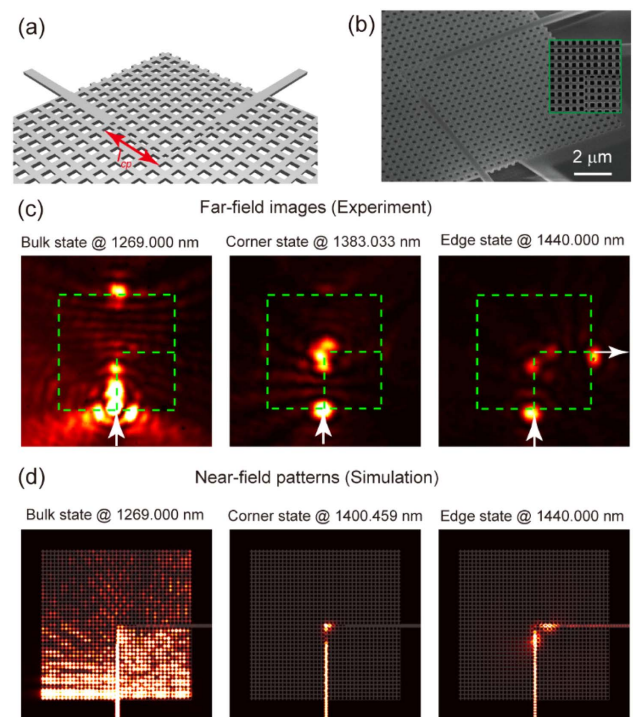


Fig. 4. Experimental observation of nanophotonic corner states through far-field images. (a) Schematic view and (b) SEM images of cross-coupled cavity based on the bend interface of SOTPC. Note that some edge rectangular holes are filled with silicon to form a line-defect photonic crystal waveguide. (c) Far-field images of bulk, edge, and corner states in a cross-coupled cavity sample via an optical microscope system. (d) Simulated field patterns of electromagnetic energy of bulk, edge, and corner states at the z center plane.

gives the far-field microscope images of a cross-coupled cavity excited by three typical wavelengths, in correspondence with bulk, edge, and corner states of bend interface. For the far-field radiation pattern at $\lambda = 1383.033$ nm, we do indeed observe the in-plane confined mode localized around the corner of the bend interface (i.e., the topological corner state). On the contrary, the excitation of the edge state at $\lambda = 1440.000$ nm would smoothly propagate along the interface without out-of-plane scattering near the corner, while the bulk state at $\lambda = 1269.000$ nm coupled to the extended slab mode and thus produced a wide range of vertical radiation inside the bulk crystals. Appendix C provides more details about the far-field images. It also confirms that all of our experimental results are in good agreement with the simulated near-field images at $z = 0$ plane [as in Fig. 4(d)], regardless of the blue shift of the operation wavelength. This cross-coupled cavity design enables us to experimentally “see” the topological corner states on the PC slab.

D. Q-Factor Measurement of the Corner State in a Cross-Coupled Cavity

Apart from the far-field observation of the corner state, it is necessary to deeply study the optical properties and coupling mechanism of the cross-coupled cavity. In this section, we will use the temporal coupled-mode theory (CMT) [2,43,44] to

further study the optical properties of the above cross-coupled cavity, which can be modeled as shown in the schematic diagram of Fig. 5(a). In CMT, the cavity mode with field amplitude A has three attenuation mechanisms that are characterized by their lifetimes (i.e., τ_r radiated to free space and τ_{w1}/τ_{w2} coupled to input/output waveguides 1/2). s_{1+}/s_{1-} and s_{2+}/s_{2-} are input/output field amplitudes for input waveguide 1 and output waveguide 2, respectively. As detailed in Appendix D, we can solve the temporal coupled-mode equations [see Eqs. (D1)–(D3) in Appendix D] and retrieve the cross-coupled cavity transmittance with Lorentz features described by

$$T(\lambda) = \frac{Q_r^2}{4Q_r^2 Q_w^2 (\lambda_C/\lambda - 1)^2 + (Q_r + Q_w)^2}, \quad (3)$$

where $Q_r = \pi c \tau_r / \lambda_C$ is the out-of-plane radiative quality factor and $Q_w = \pi c \tau_{w1} / (2\lambda_C) = \pi c \tau_{w2} / (2\lambda_C)$ is the in-plane coupling quality factor of the cross-coupled cavity, respectively. λ_C is the central wavelength at a Lorentz peak for the resonant cavity mode. In Fig. 5(b), we give the full-wave simulated

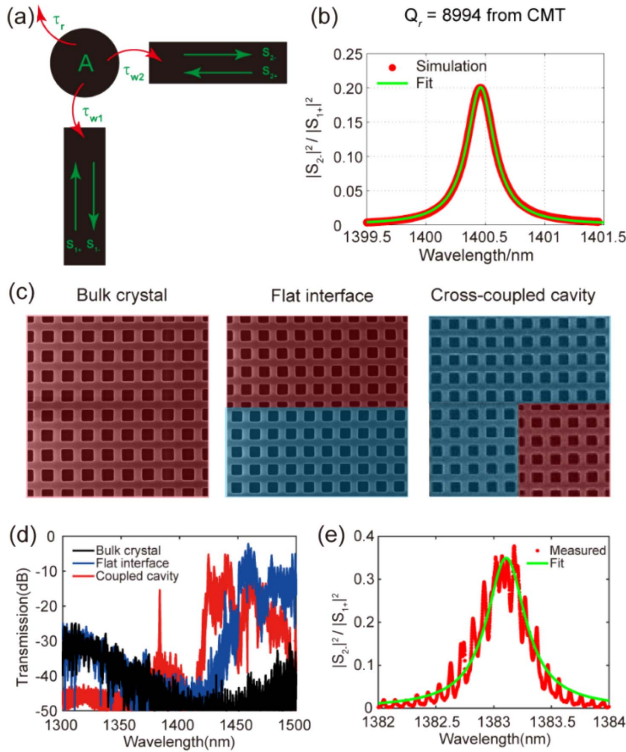


Fig. 5. Measurement of transmission spectra and Q factor in a cross-coupled cavity. (a) Description of cross-coupled cavity mode by temporal CMT with Lorentz feature. (b) Simulated transmittance (red dots) and Lorentz fitting (green line) of cross-coupled cavity, that retrieve the resonant wavelength $\lambda_C = 1400.459$ nm, the out-of-plane radiative quality factor $Q_r = 8994$, and the in-plane coupling quality factor $Q_w = 11,069$ for the designed cavity. (c) SEM images of fabricated samples and (d) measured transmission spectra for bulk crystal, flat interface, and cross-coupled cavity, respectively. The resonant peak near 1383 nm is in correspondence with topological corner state. (e) Measured transmission spectrum (red) of cross-coupled cavity around the resonant wavelength, normalized by the transmission spectrum of a line-defect PC waveguide.

transmittance (red dots) of the cross-coupled cavity. By the Lorentz curve fitting [as a green line in Fig. 5(b)] of Eq. (3), we have $\lambda_C = 1400.459$ nm, $Q_r = 8994$, and $Q_w = 11,069$ for our designed cavity. It validates that CMT is available to describe the light confinement of topological corner state, because the value of Q_r is very close to the intrinsic quality factor of bend interface in Fig. 3(c). Note that the fitting λ_C has a slight deviation from that of bend interface due to the effect on the coupled waveguide.

In the experiment, Fig. 5(c) gives the SEM images of fabricated samples for bulk crystal, a flat interface, and cross-coupled cavity, respectively. The shrunk/expanded PCs are labeled as blue/red false color. The measured transmission spectra of bulk crystal (black), flat interface (blue), and cross-coupled interface (red) samples are shown in Fig. 5(d), which is normalized by the transmission spectra of a strip Si waveguide. In the low-transmission region of bulk crystal and flat interface, the spectrum of the cross-coupled cavity has a resonant peak near 1383 nm, in correspondence with the corner state. Around the resonant wavelength, we show another measured transmission spectrum of the cross-coupled cavity normalized by the transmittance of a line-defect PCW, as the red dots shown in Fig. 5(e). Based on CMT, we obtain a Lorentz fitting curve (green) to experimentally evaluate the resonant wavelength $\lambda_C = 1383.108$ nm, the in-plane coupling quality factor $Q_w = 5688$, and the out-of-plane radiative quality factor $Q_r = 8233$ (also can be considered as the intrinsic Q of corner state). These results quantitatively confirm that we have successfully obtained a high- Q cavity mode based on the topological corner state.

3. CONCLUSION

In summary, we have successfully implemented a cross-coupled PC cavity based on second-order topology and observed a topological corner state under in-plane excitation at a telecommunications wavelength. Both simulated results in the bend interface and measured results in the cross-coupled PC cavity show evidence of the topological corner state in silicon PIC. In addition, we measure the transmission spectra of the interface to characterize the optical property of the cross-coupled cavity, and retrieve the intrinsic Q via the temporal coupled-mode theory. In future, we believe it is interesting to introduce the tight-binding model of SOTPC into the temporal coupled-mode equation, and thus develop a non-Hermitian Hamiltonian to more precisely describe the radiative topological corner states. In devices, combined with the coupled cavity-waveguide design [45,46], the topological corner state is promising for cavity-mode-based passive devices (e.g., optical filters, routers, and multiplexers) in silicon PICs, and its applications for on-chip optical information transfer.

APPENDIX A: METHODS

1. Details for Numerical Simulations

All of simulation results in this work are retrieved from a suspended slab in 3D model. The maximum scale of the discrete grid is smaller than 27 nm, making the resolution large enough to ensure the convergence.

By using the eigenmode solver of the MIT Photonic Bands (MPB) [38], we setup a square-lattice photonic crystal slab to calculate the TE-like band structures and the corresponding eigenfields $H_z(k_x, k_y)$ at the in-plane wavevector $\mathbf{k} = (k_x, k_y)$. Based on the Bloch theorem that $H_z = u_n(\mathbf{k}) \exp(i\mathbf{k} \cdot \mathbf{r})$, we can retrieve the n -th-band Bloch function of eigenfields $u_n(\mathbf{k})$ to calculate the expectation value of the mirror-flip operation η_i .

On the other hand, all of the calculations for the Q factor, LDOS, and optical transport were implemented by MIT Electromagnetic Equation Propagation (MEEP) [40] based on finite-difference time-domain (FDTD) method. The perfectly matched layers (PMLs) were imposed at the boundaries of simulated domains to absorb the outcoming waves. To explore the optical properties of the corner state in Fig. 3, we put an H_z -polarized dipole source at the corner point [labeled as black dot in Fig. 3(a)] in the z center plane. For LDOS and Q -factor simulations, the dipole source is a Gaussian pulse in time domain, and the results are detected after a certain time that the dipole source has been turned off. The dipole source is a broadband pulse at the frequency center $f_c = 0.307c/a$ with the bandwidth $\Delta f = 0.1c/a$. We obtained the LDOS spectrum at the corner point after $30000a/c$ additional time that the dipole source has been turned off. Such a simulated setup can ensure the output results to get rid of the effects on the source itself. On the other hand, the dipole source is a continuous wave at the resonant frequency for the simulation of field patterns.

2. Process of Sample Fabrication

The experimental samples were manufactured by employing a top-down nanofabrication process on an SOI wafer (with a nominal 220 nm device layer and 2.0 μm buried oxide layer). First, a 370 nm thickness positive resist (ZEP520A) was spun with a rotating speed of 3500 min^{-1} on the wafer, and dried for 10 min at 180°C . The PC patterns were defined by electron-beam lithography (EBPG5000 ES, Vistec) in the resist, and developed by dimethylbenzene for 70 s. Second, an inductively coupled plasma (ICP) etching step was applied to etch the PC structures and coupling waveguides on the top 220 nm thick silicon layer. Then the resist was removed by using an ultrasonic treatment process at room temperature. The final step was to hollow out the substrate SiO_2 layer below PCs, using HF_4 to avoid TE–TM coupling.

3. Schematic View of the Experimental Setup

Figure 6 depicts the experimental setup for the measurement of transmission spectra and far-field microscopy images. The optical sources were generated from three tunable continuous wave (CW) lasers (Santec TSL-550/710) at a telecom wavelength (1260–1640 nm). The incident light was firstly launched into a fiber polarization controller to select the TE wave, and then coupled to the input waveguide with the aid of a polarization-maintaining lensed fiber. After passing through SOTPC devices, the output signals were mainly divided into two paths. One is the in-plane propagating waves that coupled to the output waveguide and were collected by another lensed fiber. By automatically tuning the wavelength of CW laser with scanning step 10 pm, the transmission spectra

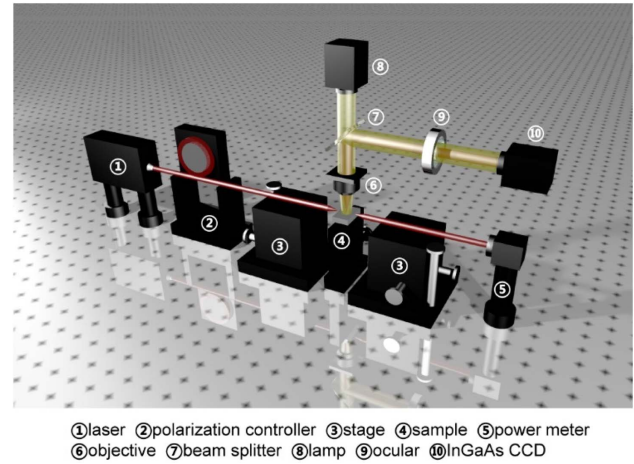


Fig. 6. Schematic diagram of the experimental setup.

were detected by an optical power meter (MPM-210). The other is the out-of-plane radiation that the propagating waves scattered into the z direction and was collected by a $100\times$ microscope objective. Then the far-field patterns could be imaged by using an InGaAs CCD (Xenics Bobcat-640-GigE).

APPENDIX B: OPENING THE PHOTONIC BANDGAP BY CLUSTER SHRINKAGE/EXPANSION

The unit cell of photonic crystal (PC) in this work consists of four air-hole clusters in the silicon background, as depicted in Fig. 7(a). d_x (d_y) is the distance of two intra-clusters along x (y) direction, whereas the nearest inter-cluster distance is $a - d_x$ ($a - d_y$). a is the lattice constant of PC. Next, we will study the evolution of photonic bands with cluster shrinkage/expansion.

To simplify, the band structures in this section are calculated from a 2D effective model with the background refractive

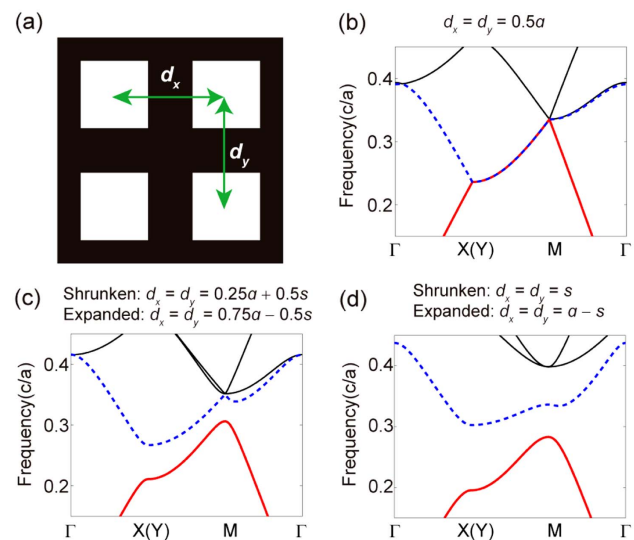


Fig. 7. Evolution of photonic band structures with cluster shrinkage/expansion. (a) Schematic view of the photonic crystal unit cell, consisting of four air-hole clusters. (b)–(d) TE band structures with different intra-cluster distance.

index $n_{\text{eff}} = 2.88$, by using MPB. For $d_x = d_y = 0.5a$ in Fig. 7(b), the first (red solid) and second (blue dashed) TE bands have a double degenerated line along the Brillouin zone boundary (i.e., $X-M$). When we shrink/expand the clusters to the center/corner of unit cell, the degenerated bands along the $X-M$ line will split into two nondegenerate bands, as shown in Fig. 7(c). In terms of the specific condition that $d_x = d_y = s$ (or $d_x = d_y = a - s$), the intra-clusters (or inter-clusters) can be reconsidered as a new square hole with side length doubled to $2s$. In this case, the band structure in Fig. 7(d) shows an omnidirectional TE gap between the first (red solid) and second (green dashed) TE bands.

In PCs, it is common sense that the spatial Fourier components of cavity mode are related to the origin of bandgap opening. For our case shown in Fig. 7, the topological bandgap opens from a double degenerated $X-M$ line. Therefore, the wavevector components of the corner state are mainly distributed along the Brillouin zone boundary [see Fig. 3(d)]. On the other hand, the corner state will be affected by the edge states of interface. The effects can be divided into two channels: one is from down to right that can induce upward right “momentum”; another is from left to down that can induce downward left “momentum.” As a consequence, the wavevector components of the corner state will be enhanced at the upward right and downward left M points [see Fig. 3(d)].

APPENDIX C: DETAILS FOR FAR-FIELD IMAGES OF THE CROSS-COUPLED CAVITY

In this section, we will show more details about the experiments of cross-coupled cavity. The far-field microscope images in Figs. 8(a)–8(c) imply three typical results for our cross-coupled cavity (i.e., excitation of bulk state at $\lambda = 1269$ nm, edge state at $\lambda = 1440$ nm, and corner state at $\lambda = 1383.033$ nm), which have been demonstrated in the main text in Fig. 4(c). Furthermore, Fig. 8(d) shows a far-field image at $\lambda = 1301$ nm where the incident light cannot couple into the PC region, because the operation wavelength is away from the corner state

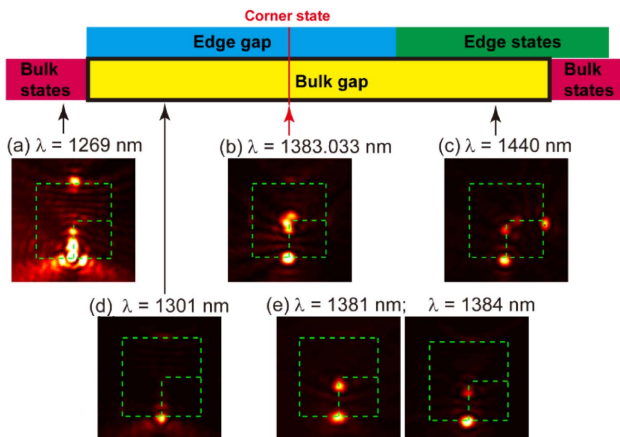


Fig. 8. Far-field images of cross-coupled cavity, under in-plane excitation of (a) bulk state at $\lambda = 1269$ nm, (b) corner state at $\lambda = 1383.033$ nm, (c) edge state at $\lambda = 1440$ nm and without eigenmode excitation of PC slab (d) at $\lambda = 1301$ nm and (e) at the resonant wavelength, respectively.

and the band edge of the bulk states. In Fig. 8(e), considering the operation wavelengths at $\lambda = 1381$ nm and $\lambda = 1384$ nm that slightly deviate from the corner state, the far-field images manifest strong scattering at the end facet between the line-defect PC waveguide and the bend interface, indicating a lack of eigenmode excitation of the PC slab.

APPENDIX D: TEMPORAL COUPLED-MODE THEORY

Here is a detailed deduction about the temporal coupled-mode theory (CMT) for the description of our cross-coupled cavity. The CMT model is schematically shown in the main text in Fig. 5(a). Here we only consider a weak coupling where the incident light oscillates at a fixed frequency ω near the resonant frequency ω_c . The cavity mode with a field amplitude A has three attenuation mechanisms that are characterized by their lifetimes (i.e., τ_r radiated to free space and τ_{w1}/τ_{w2} coupled to input/output waveguides $1/2$). s_{1+}/s_{1-} and s_{2+}/s_{2-} are the input/output field amplitudes for input waveguide 1 and output waveguide 2, respectively. The temporal coupled-mode equations for this two-port system can be written as

$$\frac{dA}{dt} = -i\omega_c A - A \left(\frac{1}{\tau_r} + \frac{1}{\tau_{w1}} + \frac{1}{\tau_{w2}} \right) + \left(\sqrt{\frac{2}{\tau_{w1}}} s_{1+} + \sqrt{\frac{2}{\tau_{w2}}} s_{2+} \right), \quad (\text{D1})$$

$$s_{1-} = -s_{1+} + \sqrt{2/\tau_{w1}} A, \quad (\text{D2})$$

$$s_{2-} = -s_{2+} + \sqrt{2/\tau_{w2}} A. \quad (\text{D3})$$

For simplification, we consider three conditions. (1) In a linear system, the frequency is conserved, so that the field should oscillate as time-harmonic form $e^{-i\omega t}$ and $dA/dt = i\omega A$. (2) Due to the inversion of cavity geometry, the cavity mode has equal decay rates into the two waveguides (i.e., $\tau_w = \tau_{w1} = \tau_{w2}$). (3) We only discuss the incidence of waveguide 1 and there is no input power from waveguide 2 (i.e., $s_{2+} = 0$). Substituting above conditions into Eqs. (D1) and (D3), we obtain

$$-i\omega A = -i\omega_c A - A \left(\frac{1}{\tau_r} + \frac{2}{\tau_w} \right) + \sqrt{\frac{2}{\tau_w}} s_{1+}, \quad (\text{D4})$$

$$s_{2-} = \sqrt{2/\tau_w} A. \quad (\text{D5})$$

Therefore, the transmission spectrum can be retrieved as

$$T(\omega) = \frac{|s_{2-}|^2}{|s_{1+}|^2} = \frac{2|A|^2/\tau_w}{|s_{1+}|^2} = \frac{4/\tau_w^2}{(\omega - \omega_c)^2 + (1/\tau_r + 2/\tau_w)^2}. \quad (\text{D6})$$

It means the transmittance is a Lorentz profile as a function of ω with a peak at $\omega = \omega_c$. In correspondence with the experiment, the independent variable ω is converted into

the wavelength λ through the well-known relationship of $\lambda = 2\pi c/\omega$. On the other hand, we are more concerned with the quality factor Q instead of lifetime τ . Here, $Q_r = \pi c\tau_r/\lambda_C$ is the out-of-plane radiative quality factor and $Q_w = \pi c\tau_{w1}/(2\lambda_C) = \pi c\tau_{w2}/(2\lambda_C)$ is the in-plane coupling quality factor of the cross-coupled cavity, respectively. λ_C is the central wavelength at Lorentz peak for the resonant cavity mode. In this case, the transmission spectrum of Eq. (D6) becomes

$$T(\lambda) = \frac{Q_r^2}{4Q_r^2Q_w^2(\lambda_C/\lambda - 1)^2 + (Q_r + Q_w)^2}. \quad (\text{D7})$$

To retrieve the transmission spectrum in the simulation and experiment, we should obtain the input power $|s_{1+}|^2$ and output power $|s_{2-}|^2$ of the cross-coupled cavity. It is easy to directly measure the output power $|s_{2-}|^2$ from the cross-coupled cavity sample, while the input power $|s_{1+}|^2$ is equivalent to the output power from the line-defect PC waveguide. By fitting the transmittance data as a Lorentz curve of Eq. (D7), we can have the coefficients λ_C , Q_r , and Q_w to insightfully analyze the resonant and coupling features.

Funding. National Key Research and Development Program of China (2019YFB2203502); National Natural Science Foundation of China (62035016, 11904421, 61775243, 11761161002, 12074443); Natural Science Foundation of Guangdong Province (2018B030308005, 2018A030310089); Guangdong Basic and Applied Basic Research Foundation (2019B151502036); Guangzhou Science and Technology Program key projects (201804020029); Guangzhou Science, Technology and Innovation Commission (202002030322); China Postdoctoral Science Foundation (2018M633206).

Disclosures. The authors declare no conflicts of interest.

Data availability. Data underlying the results presented in this paper are not publicly available at this time but may be obtained from the authors upon reasonable request.

[†]These authors contributed equally to this paper.

REFERENCES

- K. J. Vahala, "Optical microcavities," *Nature* **424**, 839–846 (2003).
- J. D. Joannopoulos, S. G. Johnson, J. N. Winn, and R. D. Meade, *Photonic Crystals: Molding the Flow of Light* (Princeton University, 2011).
- Y. Akahane, T. Asano, B.-S. Song, and S. Noda, "High-Q photonic nanocavity in a two-dimensional photonic crystal," *Nature* **425**, 944–947 (2003).
- F. Haldane and S. Raghu, "Possible realization of directional optical waveguides in photonic crystals with broken time-reversal symmetry," *Phys. Rev. Lett.* **100**, 013904 (2008).
- L. Lu, J. D. Joannopoulos, and M. Soljacic, "Topological photonics," *Nat. Photonics* **8**, 821–829 (2014).
- T. Ozawa, H. M. Price, A. Amo, N. Goldman, M. Hafezi, L. Lu, M. C. Rechtsman, D. Schuster, J. Simon, O. Zilberberg, and I. Carusotto, "Topological photonics," *Rev. Mod. Phys.* **91**, 015006 (2019).
- L.-H. Wu and X. Hu, "Scheme for achieving a topological photonic crystal by using dielectric material," *Phys. Rev. Lett.* **114**, 223901 (2015).
- Y. Yang, Y. F. Xu, T. Xu, H. X. Wang, J. H. Jiang, X. Hu, and Z. H. Hang, "Visualization of a unidirectional electromagnetic waveguide using topological photonic crystals made of dielectric materials," *Phys. Rev. Lett.* **120**, 217401 (2018).
- J.-W. Dong, X.-D. Chen, H. Zhu, Y. Wang, and X. Zhang, "Valley photonic crystals for control of spin and topology," *Nat. Mater.* **16**, 298–302 (2017).
- T. Ma and G. Shvets, "All-Si valley-Hall photonic topological insulator," *New J. Phys.* **18**, 025012 (2016).
- X.-D. Chen, F.-L. Zhao, M. Chen, and J.-W. Dong, "Valley-contrasting physics in all-dielectric photonic crystals: orbital angular momentum and topological propagation," *Phys. Rev. B* **96**, 020202 (2017).
- X.-D. Chen, W.-M. Deng, F.-L. Shi, F.-L. Zhao, M. Chen, and J.-W. Dong, "Direct observation of corner states in second-order topological photonic crystal slabs," *Phys. Rev. Lett.* **122**, 233902 (2019).
- B.-Y. Xie, G.-X. Su, H.-F. Wang, H. Su, X.-P. Shen, P. Zhan, M.-H. Lu, Z.-L. Wang, and Y.-F. Chen, "Visualization of higher-order topological insulating phases in two-dimensional dielectric photonic crystals," *Phys. Rev. Lett.* **122**, 233903 (2019).
- S. Barik, A. Karasahin, C. Flower, T. Cai, H. Miyake, W. DeGottardi, M. Hafezi, and E. Waks, "A topological quantum optics interface," *Science* **359**, 666–668 (2018).
- X. T. He, E. T. Liang, J. J. Yuan, H. Y. Qiu, X. D. Chen, F. L. Zhao, and J. W. Dong, "A silicon-on-insulator slab for topological valley transport," *Nat. Commun.* **10**, 872 (2019).
- M. I. Shalae, W. Walasik, A. Tsukernik, Y. Xu, and N. M. Litchinitser, "Robust topologically protected transport in photonic crystals at telecommunication wavelengths," *Nat. Nanotechnol.* **14**, 31–34 (2019).
- Y. Ota, F. Liu, R. Katsumi, K. Watanabe, K. Wakabayashi, Y. Arakawa, and S. Iwamoto, "Photonic crystal nanocavity based on a topological corner state," *Optica* **6**, 786–789 (2019).
- Y. Yang, Y. Yamagami, X. Yu, P. Pitchappa, J. Webber, B. Zhang, M. Fujita, T. Nagatsuma, and R. Singh, "Terahertz topological photonics for on-chip communication," *Nat. Photonics* **14**, 446–451 (2020).
- Y. Yang, Z. Jia, Y. Wu, R.-C. Xiao, Z. H. Hang, H. Jiang, and X. C. Xie, "Gapped topological kink states and topological corner states in honeycomb lattice," *Sci. Bull.* **65**, 531–537 (2020).
- B. Bahari, A. Ndao, F. Vallini, A. El Amili, Y. Fainman, and B. Kanté, "Nonreciprocal lasing in topological cavities of arbitrary geometries," *Science* **358**, 636–640 (2017).
- A. B. Khanikaev and G. Shvets, "Two-dimensional topological photonics," *Nat. Photonics* **11**, 763–773 (2017).
- M. Kim, Z. Jacob, and J. Rho, "Recent advances in 2D, 3D and higher-order topological photonics," *Light Sci. Appl.* **9**, 130 (2020).
- D. Smirnova, A. Tripathi, S. Kruk, M. S. Hwang, H. R. Kim, H. G. Park, and Y. Kivshar, "Room-temperature lasing from nanophotonic topological cavities," *Light Sci. Appl.* **9**, 127 (2020).
- Z.-Q. Yang, Z.-K. Shao, H.-Z. Chen, X.-R. Mao, and R.-M. Ma, "Spin-momentum-locked edge mode for topological vortex lasing," *Phys. Rev. Lett.* **125**, 013903 (2020).
- J. Noh, W. A. Benalcazar, S. Huang, M. J. Collins, K. P. Chen, T. L. Hughes, and M. C. Rechtsman, "Topological protection of photonic mid-gap defect modes," *Nat. Photonics* **12**, 408–415 (2018).
- C. W. Peterson, W. A. Benalcazar, T. L. Hughes, and G. Bahl, "A quantized microwave quadrupole insulator with topologically protected corner states," *Nature* **555**, 346–350 (2018).
- M. Serra-Garcia, V. Peri, R. Susstrunk, O. R. Bilal, T. Larsen, L. G. Villanueva, and S. D. Huber, "Observation of a phononic quadrupole topological insulator," *Nature* **555**, 342–345 (2018).
- S. Mittal, V. V. Orre, G. Zhu, M. A. Gorlach, A. Poddubny, and M. Hafezi, "Photonic quadrupole topological phases," *Nat. Photonics* **13**, 692–696 (2019).
- X. Ni, M. Weiner, A. Alu, and A. B. Khanikaev, "Observation of higher-order topological acoustic states protected by generalized chiral symmetry," *Nat. Mater.* **18**, 113–120 (2019).
- H. Xue, Y. Yang, F. Gao, Y. Chong, and B. Zhang, "Acoustic higher-order topological insulator on a kagome lattice," *Nat. Mater.* **18**, 108–112 (2019).
- M. Li, D. Zhirihin, M. Gorlach, X. Ni, D. Filonov, A. Slobozhanyuk, A. Alù, and A. B. Khanikaev, "Higher-order topological states in photonic

- kagome crystals with long-range interactions," *Nat. Photonics* **14**, 89–94 (2019).
32. X. Xie, W. Zhang, X. He, S. Wu, J. Dang, K. Peng, F. Song, L. Yang, H. Ni, Z. Niu, C. Wang, K. Jin, X. Zhang, and X. Xu, "Cavity quantum electrodynamics with second-order topological corner state," *Laser Photon. Rev.* **14**, 1900425 (2020).
 33. W. Zhang, X. Xie, H. Hao, J. Dang, S. Xiao, S. Shi, H. Ni, Z. Niu, C. Wang, K. Jin, X. Zhang, and X. Xu, "Low-threshold topological nanolasers based on the second-order corner state," *Light Sci. Appl.* **9**, 109 (2020).
 34. C. Han, M. Kang, and H. Jeon, "Lasing at multidimensional topological states in a two-dimensional photonic crystal structure," *ACS Photon.* **7**, 2027–2036 (2020).
 35. H. R. Kim, M. S. Hwang, D. Smirnova, K. Y. Jeong, Y. Kivshar, and H. G. Park, "Multipolar lasing modes from topological corner states," *Nat. Commun.* **11**, 5758 (2020).
 36. F. Liu and K. Wakabayashi, "Novel topological phase with a zero Berry curvature," *Phys. Rev. Lett.* **118**, 076803 (2017).
 37. B.-Y. Xie, H.-F. Wang, H.-X. Wang, X.-Y. Zhu, J.-H. Jiang, M.-H. Lu, and Y.-F. Chen, "Second-order photonic topological insulator with corner states," *Phys. Rev. B* **98**, 205147 (2018).
 38. S. G. Johnson and J. D. Joannopoulos, "Block-iterative frequency-domain methods for Maxwell's equations in a planewave basis," *Opt. Express* **8**, 173–190 (2001).
 39. C. Fang, M. J. Gilbert, and B. A. Bernevig, "Bulk topological invariants in noninteracting point group symmetric insulators," *Phys. Rev. B* **86**, 115112 (2012).
 40. A. Oskooi, D. Roundy, M. Ibanescu, P. Bermel, J. D. Joannopoulos, and S. G. Johnson, "MEEP: a flexible free-software package for electromagnetic simulations by the FDTD method," *Comput. Phys. Commun.* **181**, 687–702 (2010).
 41. A. Taflov, A. Oskooi, and S. G. Johnson, *Advances in FDTD Computational Electrodynamics: Photonics and Nanotechnology* (Artech House, 2013).
 42. K. Srinivasan and O. Painter, "Momentum space design of high-Q photonic crystal optical cavities," *Opt. Express* **10**, 670–684 (2002).
 43. C. Manolatou, M. J. Khan, S. Fan, P. R. Villeneuve, H. A. Haus, and J. D. Joannopoulos, "Coupling of modes analysis of resonant channel add-drop filters," *IEEE J. Quantum Electron.* **35**, 1322–1331 (1999).
 44. Q. Li, T. Wang, Y. Su, M. Yan, and M. Qiu, "Coupled mode theory analysis of mode-splitting in coupled cavity system," *Opt. Express* **18**, 8367–8382 (2010).
 45. C.-Y. Ji, Y. Zhang, B. Zou, and Y. Yao, "Robust Fano resonance in the photonic valley Hall states," *Phys. Rev. A* **103**, 023512 (2021).
 46. A. Shi, B. Yan, R. Ge, J. Xie, Y. Peng, H. Li, W. E. I. Sha, and J. Liu, "Coupled cavity-waveguide based on topological corner state and edge state," *Opt. Lett.* **46**, 1089–1092 (2021).